Electronic Supplementary Material (ESI) for Dalton Transactions.

The Coordination Chemistry of the Neutral *Tris*-2-pyridyl Silicon Ligand [PhSi(6-Me-2-py)$_3$]

Alex J. Plajer, Annie L. Colebatch, Markus Enders, Álvaro García-Romero, Andrew D. Bond, Raúl García-Rodríguez, and Dominic S. Wright

Synthetic Procedures

General Experimental Methods

All experiments were carried out on a Schlenk-line under a nitrogen atmosphere or with the aid of a N_2-filled glove box (Saffron type α). Toluene and THF were dried under nitrogen over sodium or sodium/benzophenone, respectively, whereas acetonitrile was dried over calcium hydride. 6-methyl-2-bromo-pyridine was distilled over CaH_2 and stored over 4 Å molecular sieves. $PhSiCl_3$ was acquired from Aldrich Chemical Company and distilled prior to use. ^{1}H, ^{13}C{^{1} H} and ^{31}P{^{1}H} NMR spectra were recorded on a Bruker Avance 400 QNP or Bruker Avance 500 MHz cryo spectrometer. All spectra were recorded in d_8-toluene or CD_3CN with $SiMe_4$ (^{1}H) and H_3PO_4 (^{31}P, 85% in D_2O) as external standards. Unambiguous assignments of NMR resonances were made on the basis of 2D NMR experiments (^{1}H-^{1}H COSY, ^{1}H-^{1}H NOESY, ^{1}H-^{13}C HMQC and ^{1}H-^{13}C HMBC). Figure 6 in the main manuscript shows the labelling scheme for NMR assignments used in the Experimental Section. Elemental analysis was obtained using a Perkin Elmer 240 Elemental Analyser, and UV-visible spectra were collected on a Varian Cary 50 UV spectrometer.

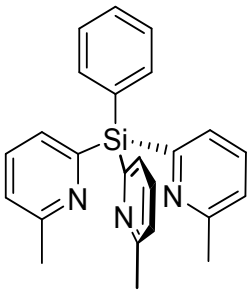

1

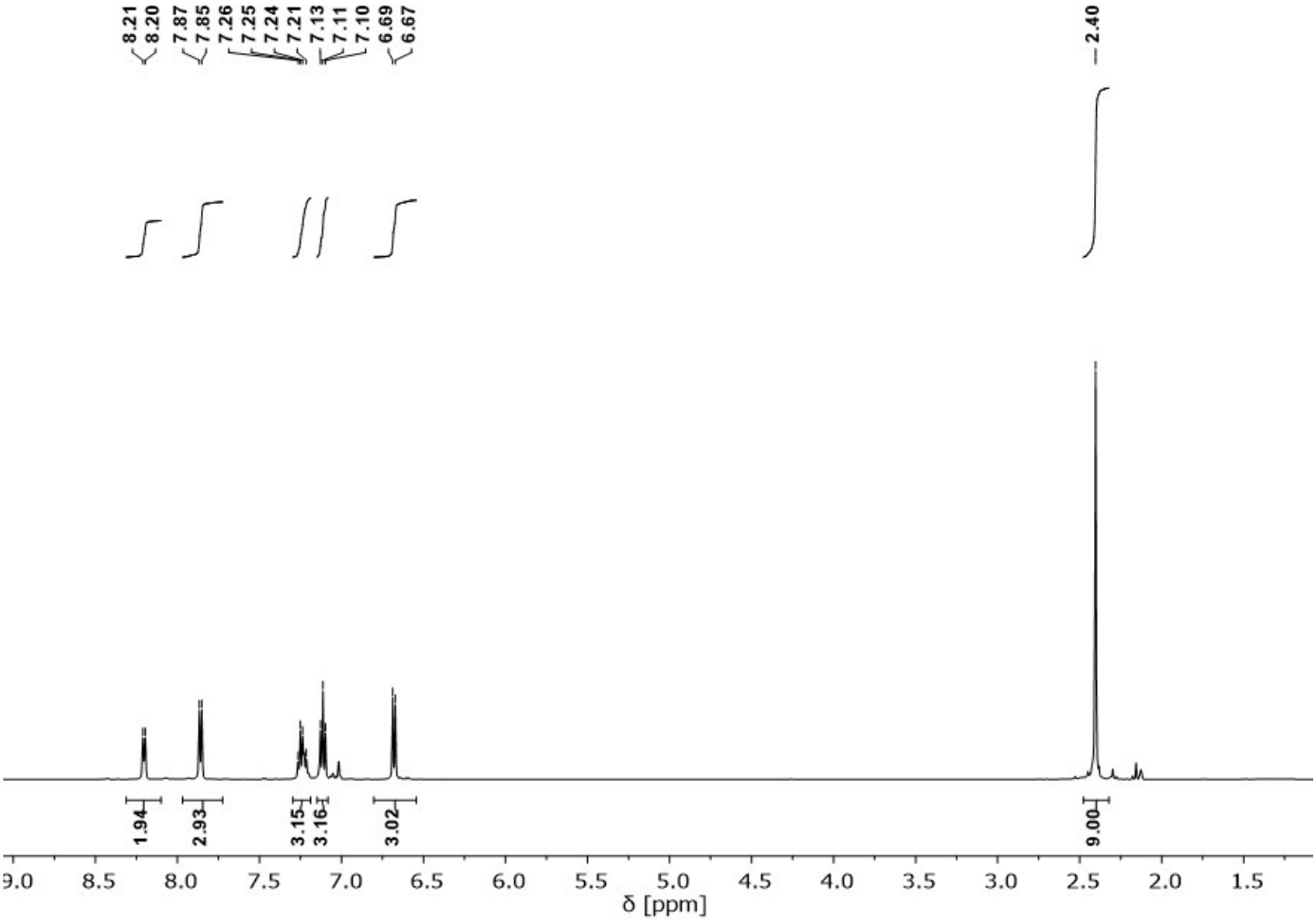

Figure S1: ^{1}H NMR spectrum (25 °C, d_8-toluene, 500.12 MHz) of **1**.

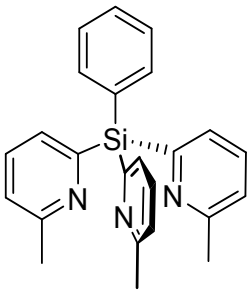

1

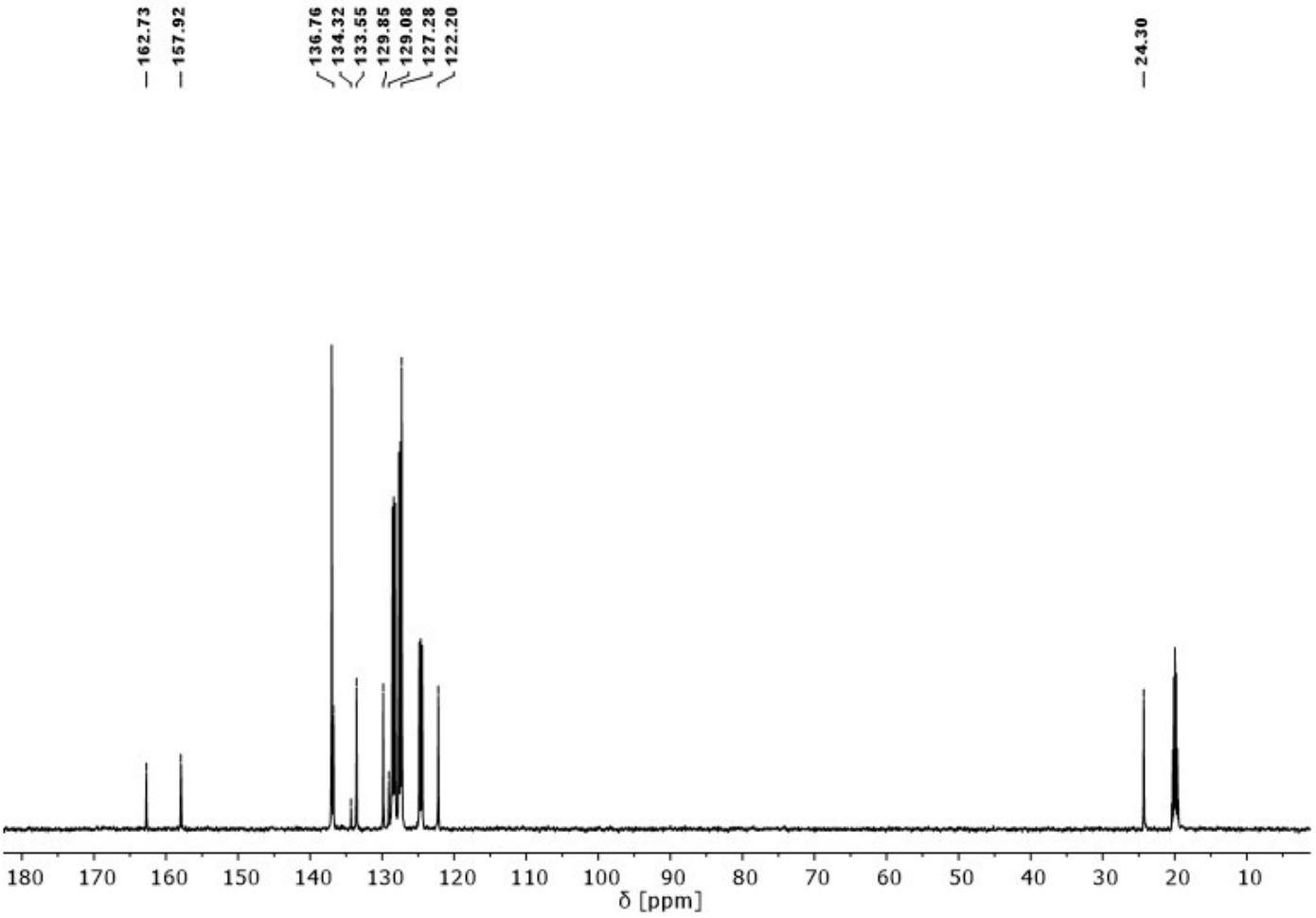

Figure S2: ^{13}C NMR spectrum (25 °C, d_8-toluene, 125.78 MHz) of **1**.

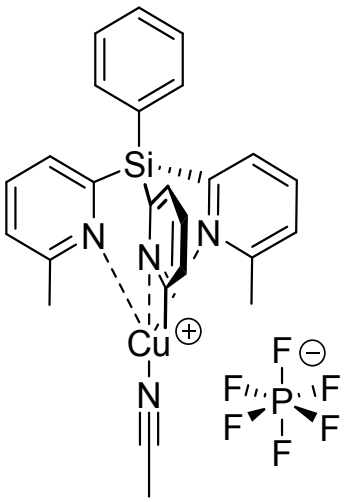

2

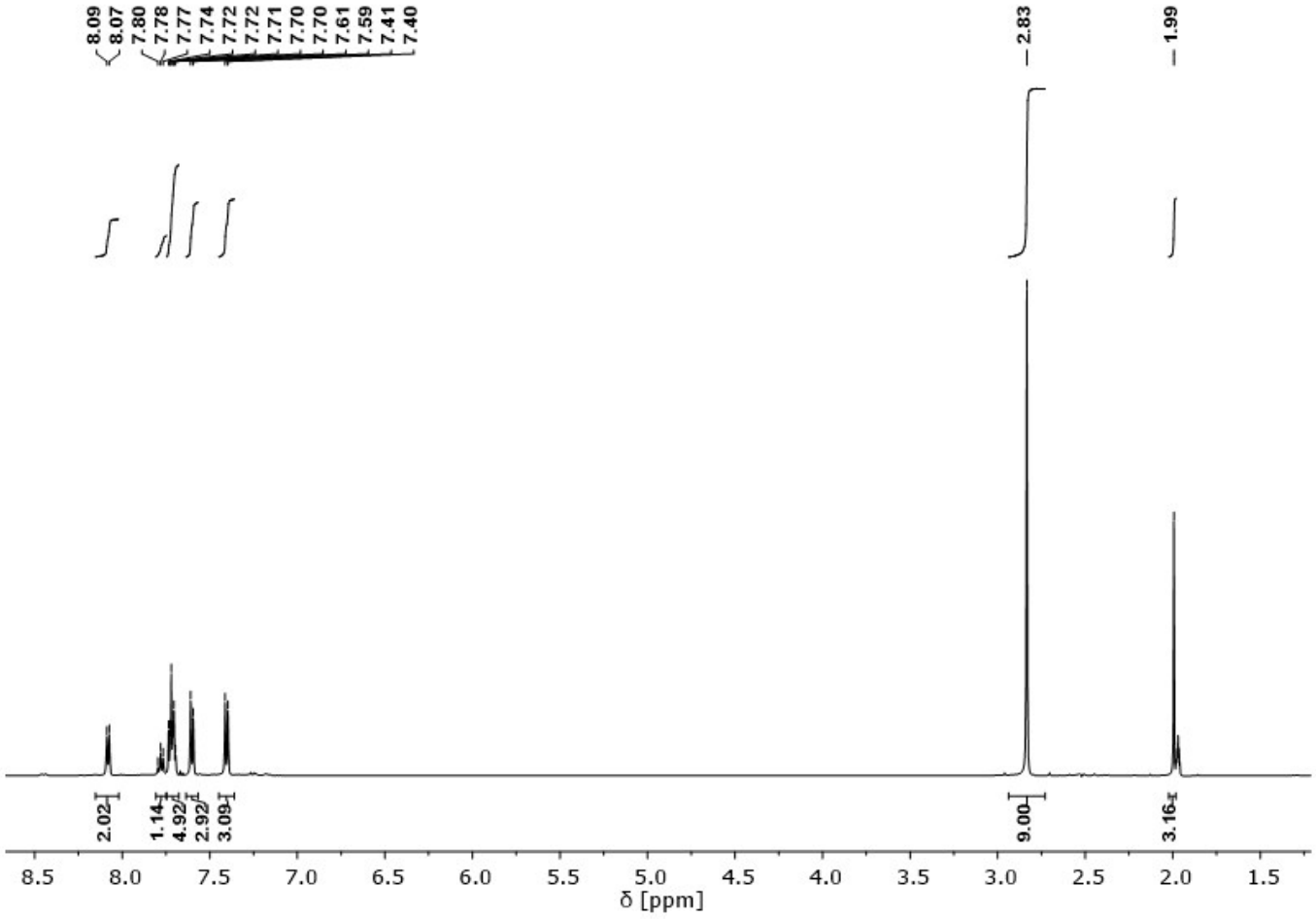

Figure S3: ^{1}H NMR spectrum (25 °C, CD_3CN, 500.12 MHz) of **2**.

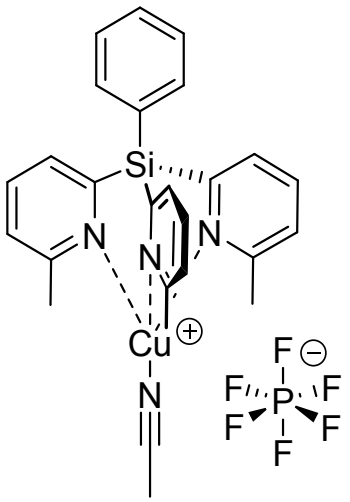

2

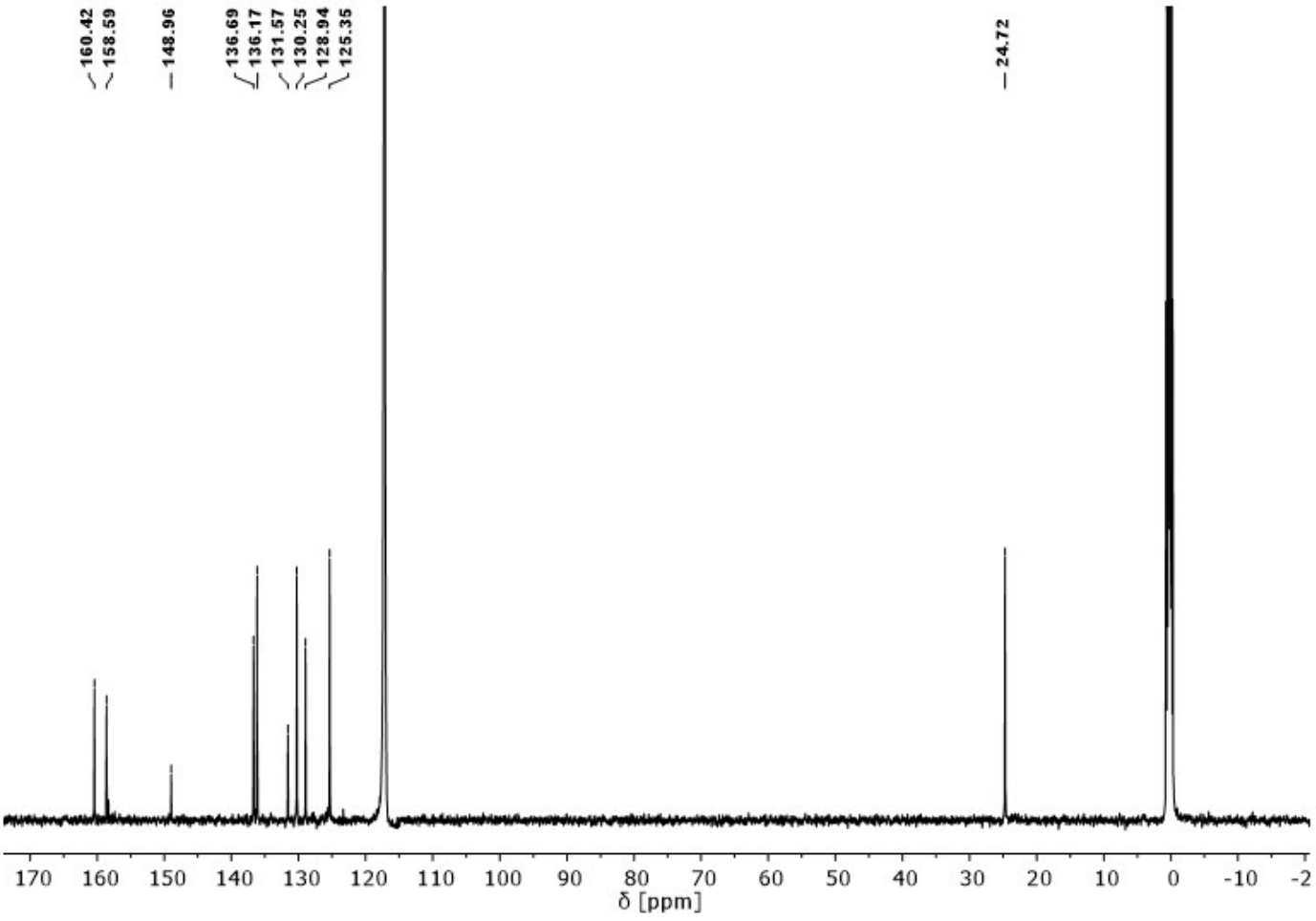

Figure S4: ^{13}C NMR spectrum (25 °C, CD_3CN, 125.78 MHz) of **2**.

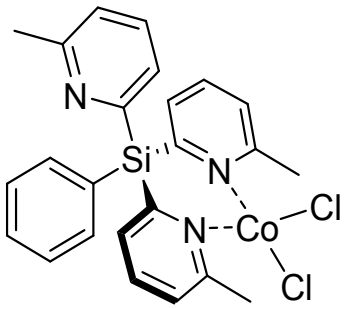

3

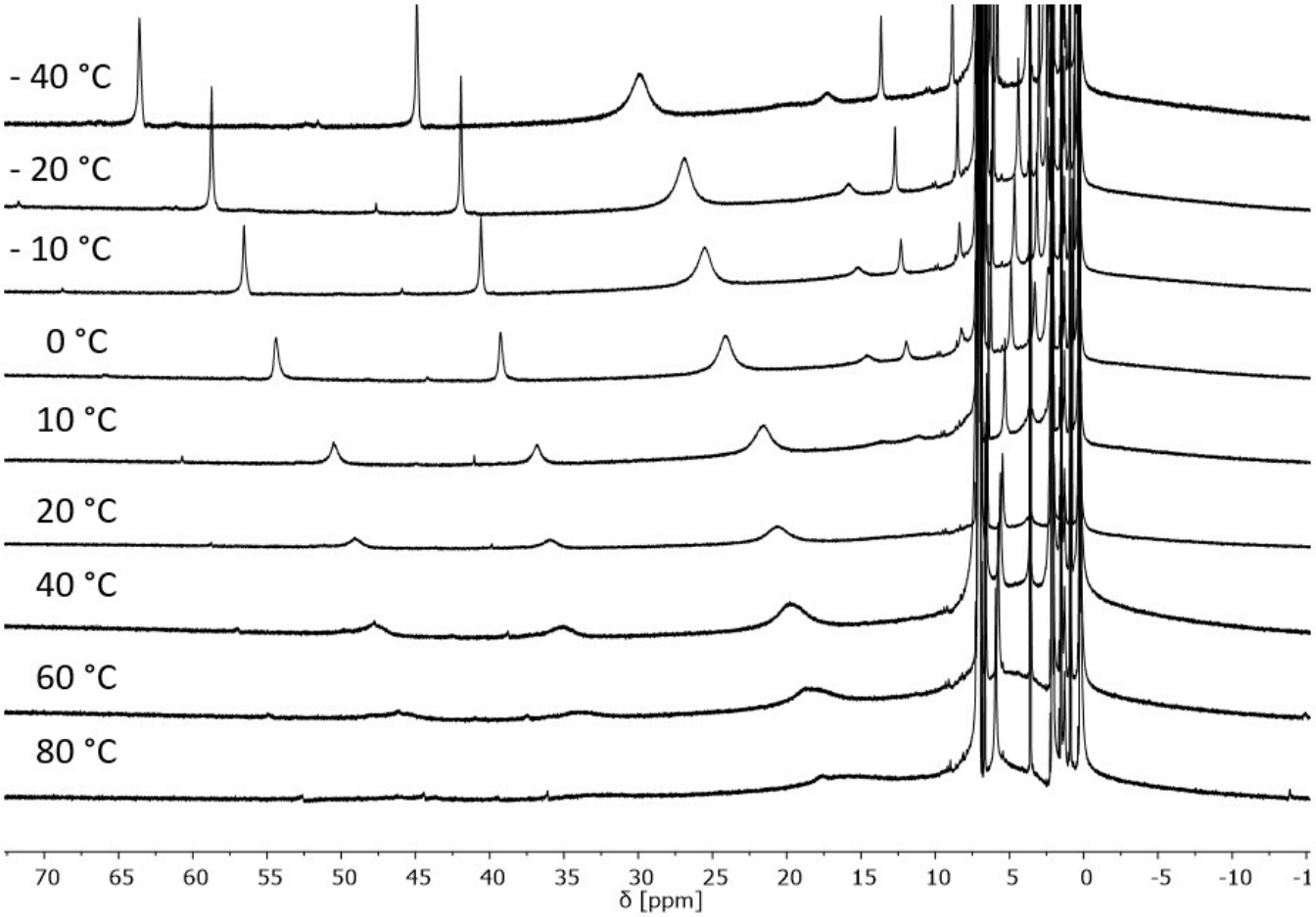

Figure S5: Variable-temperature ^{1}H NMR spectrum of paramagnetic compound **3** (d_8-toluene, 500.12 MHz) (full spectrum).

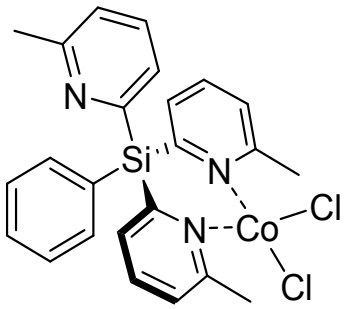

3

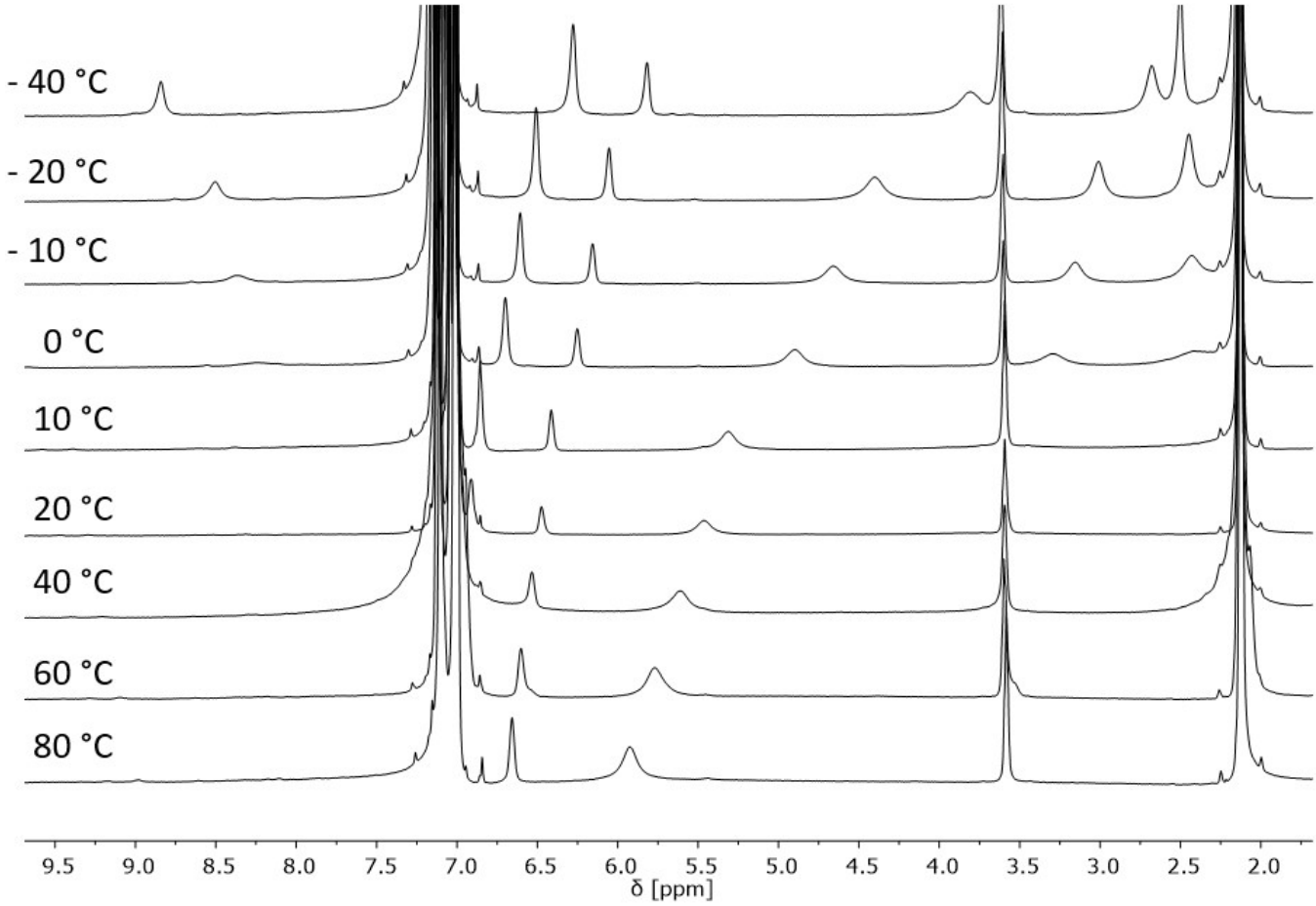

Figure S6: Variable-temperature ^{1}H NMR spectrum of paramagnetic compound **3** (d_8-toluene, 500.12 MHz) in the region *ca.* δ 2-9.5 ppm.

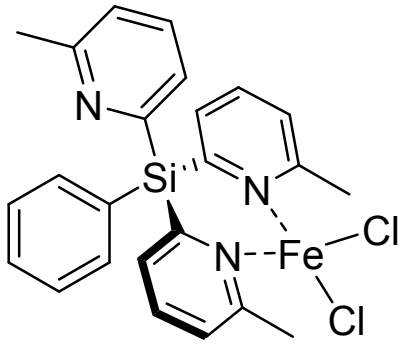

4

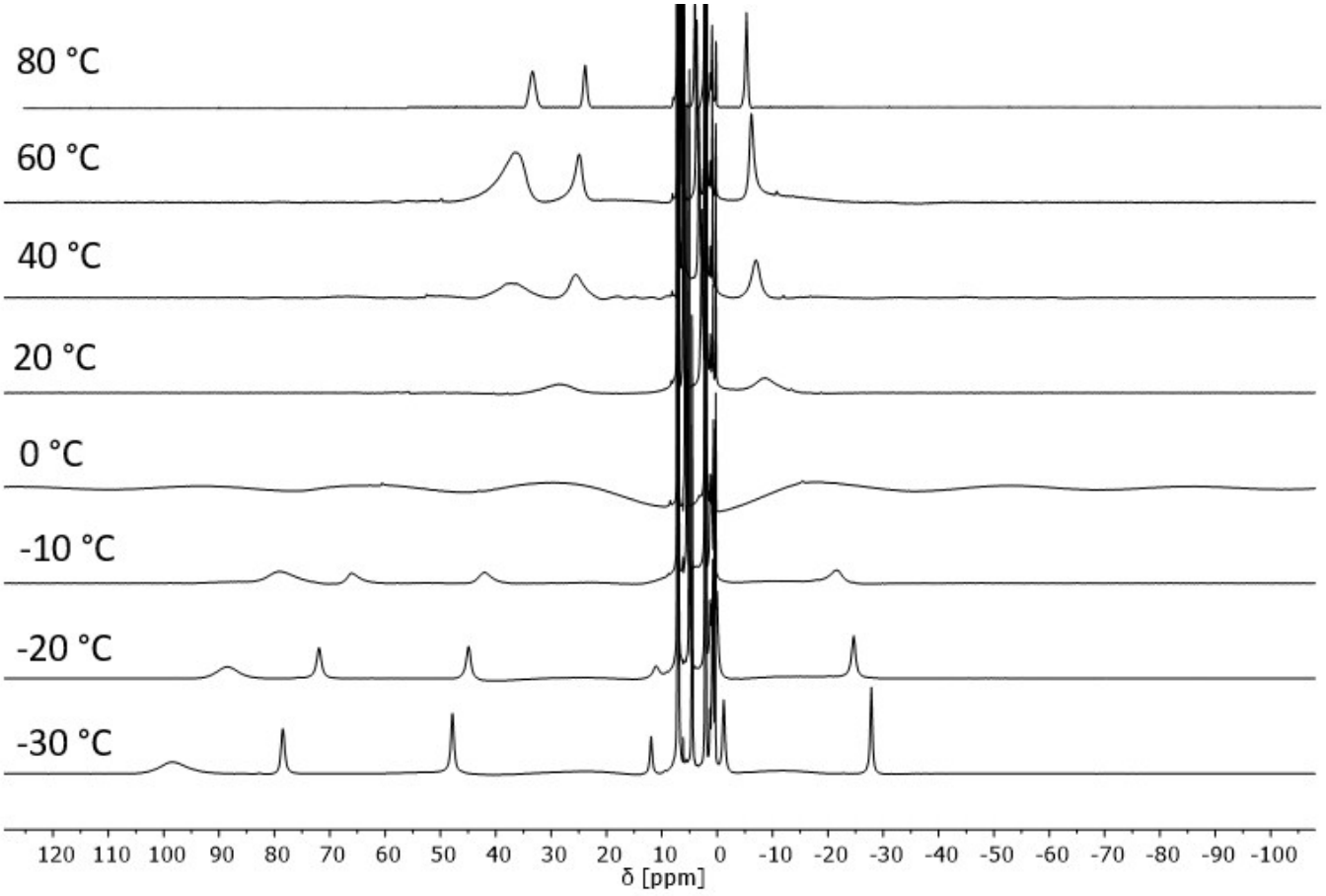

Figure S7: Variable-temperature ^{1}H NMR spectrum of paramagnetic compound **4** (d_8-toluene, 500.12 MHz) (full spectrum).

.

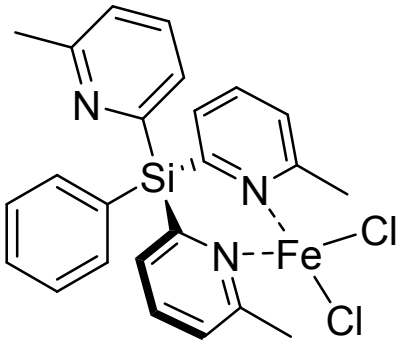

4

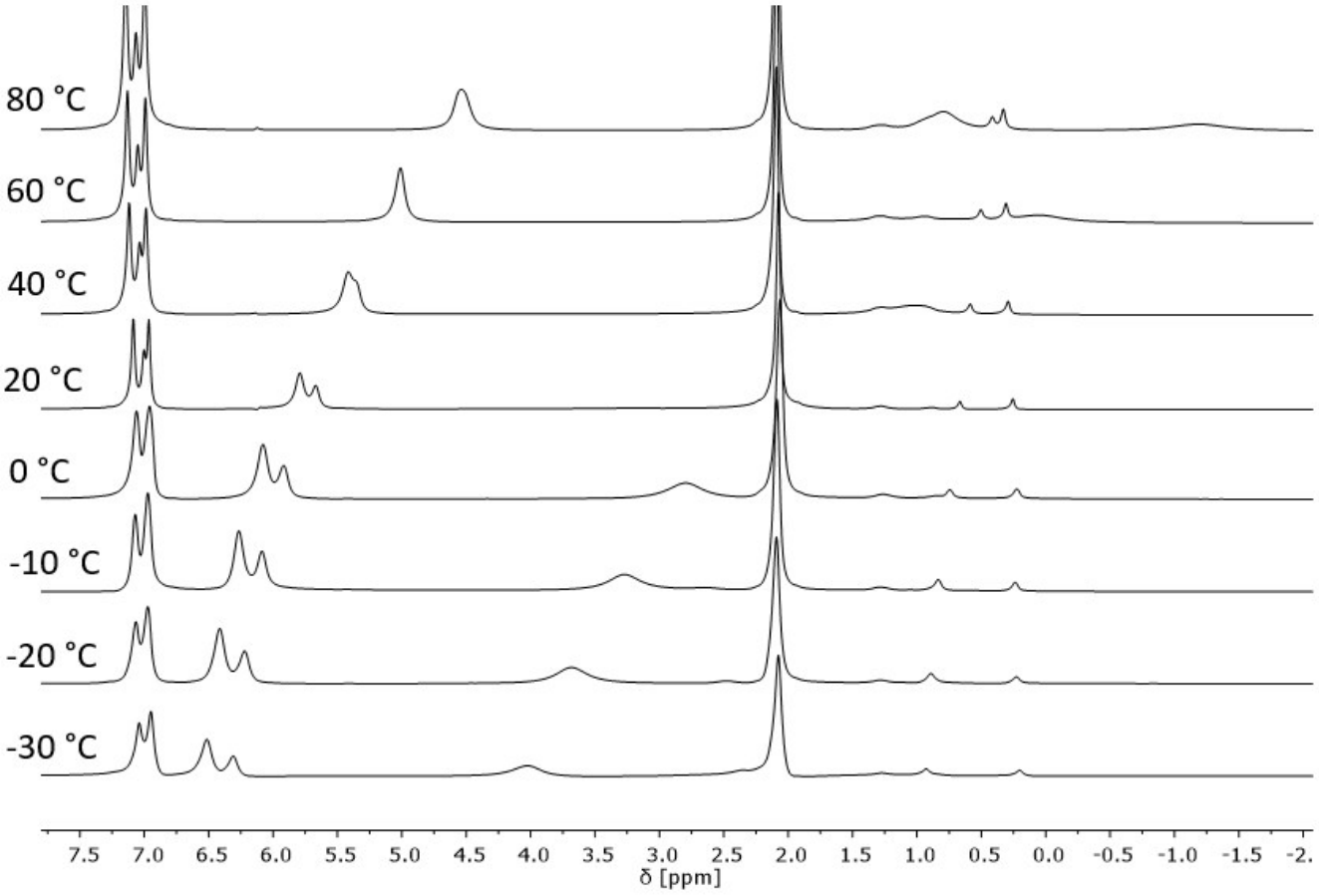

Figure S8: Variable-temperature ^{1}H NMR spectrum of paramagnetic compound **4** (d_8-toluene, 500.12 MHz) in the region ca. δ2-7.5 ppm.

Paramagnetic NMR analysis

The total NMR chemical shift is the sum of the orbital shift, the Fermi-contact shift and the pseudocontact shift according to equation S1:

$$\delta_{tot} = \delta_{orb} + \delta_{fcs} + \delta_{pcs} \qquad \text{(S1)}$$

The orbital shift is the only contribution in diamagnetic molecules whereas in paramagnetic compounds Fermi-contact and/or the pseudo-contact shift have to be considered. The first is transferred through chemical bonds and the latter is only present if the molecule is magnetically anisotropic.

Fermi-contact shifts

Starting from the solid-state molecular structures, the molecular geometries were optimized using the B3LYP/6-311G(d) level of theory in the Gaussian09 program package [1]. The Fermi-contact shifts were then obtained from the calculated spin densities by using eq. S2.

$$\delta_{con} = \frac{\mu_0 \mu_\beta^2 g_e^2}{9k} \cdot \frac{S+1}{T} \cdot \rho_{\alpha\beta} \qquad \text{with} \qquad \frac{\mu_0 \mu_\beta^2 g_e^2}{9k} = 23.5\ x\ 10^6\ [ppm\ K^{-1}] \qquad \text{(S2)}$$

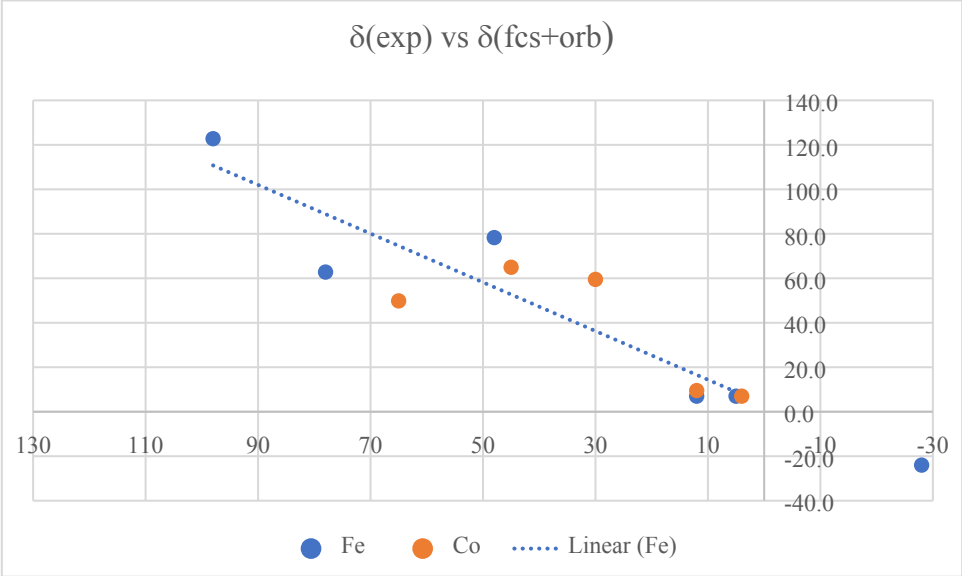

Figure S9: Correlation of experimental (horizontal) and calculated (vertical) NMR shifts (Fermi-contact and orbital contribution only).

As can be seen from Figure S9, the experimental NMR shifts are not reproduced very well by the calculated shifts when only the Fermi-contact and orbital shift are considered. Exchanging the assignments of H^1 and H^3 in both complexes leads to a somewhat better but still unsatisfactory correlation. The correct assignment becomes clear when pseudo-contact shifts are included.

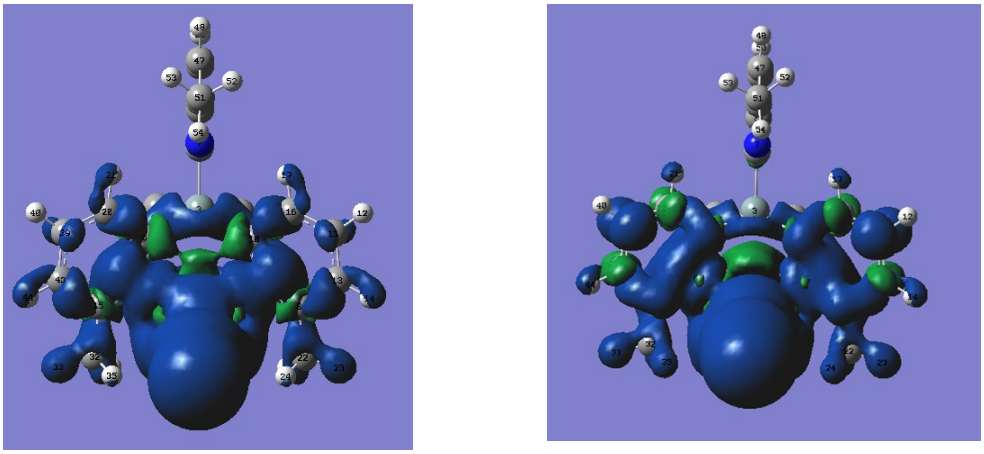

Figure S10: Plot of spin-densities from DFT calculations of **3** (left) and **4** (right).

Pseudocontact shift

In **4** the signal at +12 ppm can be assigned unambiguously to H^2 of the non-coordinated pyridyl group (H^2_{nc}) due to a cross peak in the EXSY spectrum at 230 K (Figure S11). As this atom is seven bonds away from the paramagnetic Fe centre, no Fermi contact is expected. This assumption is supported by the DFT calculation (no spin-density at this position). Consequently, the NMR shift of H^2_{nc} is the sum of the orbital shift and a pseudocontact shift of approximately +5 ppm. From this pseudocontact shift the magnetic anisotropy ($\Delta\chi_{ax}$) can be calculated using eq. S3:

$$\delta_{pcs} = \frac{1}{12\pi} \cdot \Delta\chi_{ax} \cdot \frac{3cos^2\theta - 1}{r^3} \qquad \text{(S3)}$$

where $\Delta\chi_{ax}$ is the axial component of the magnetic anisotropy tensor, θ is the angle between the magnetic main axis and the line connecting the paramagnetic centre and the NMR nucleus, and *r* is the distance between the paramagnetic centre and the NMR nucleus.

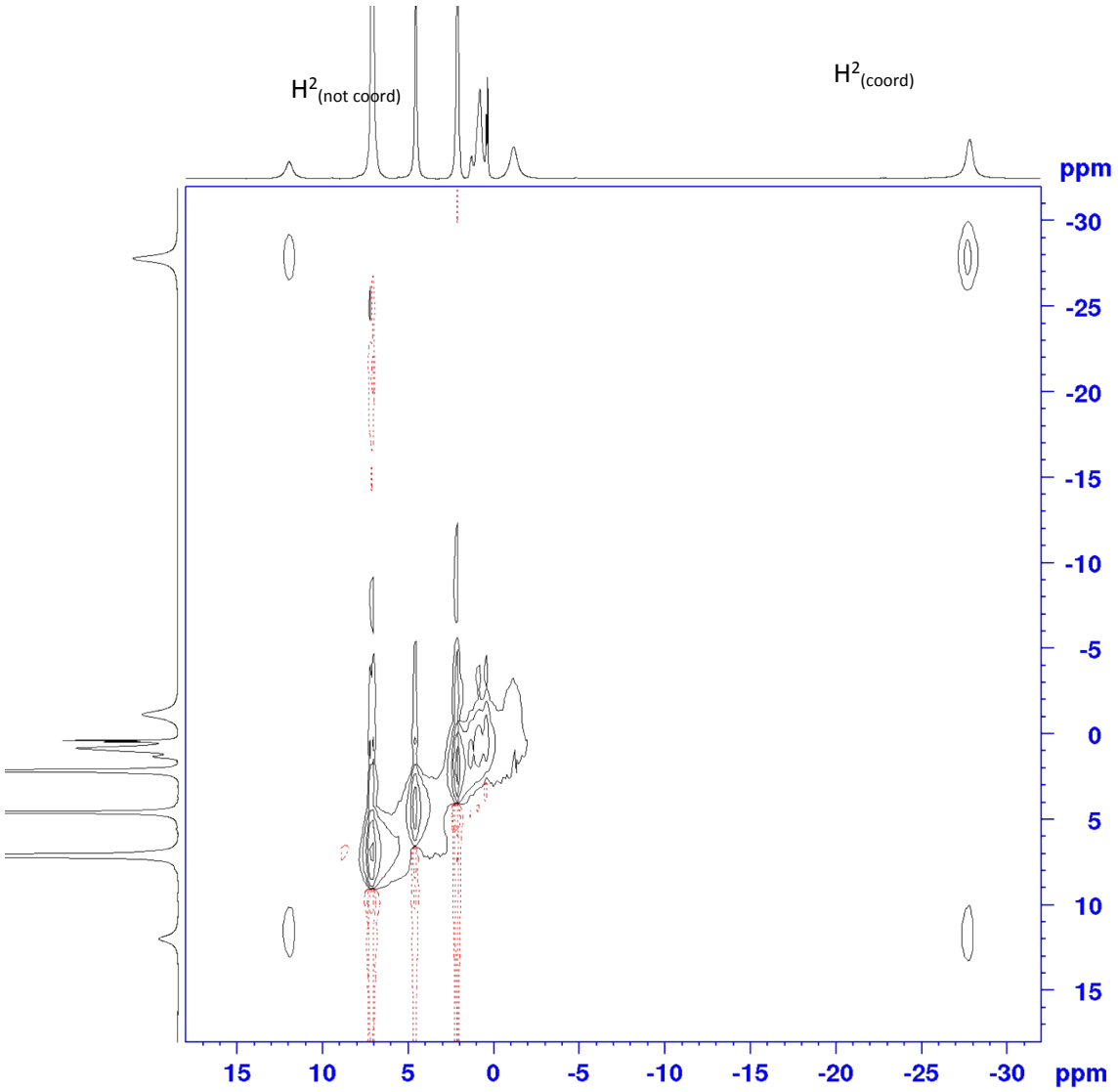

Figure S11: ^{1}H EXSY spectrum of **4** at 230 K (400 MHz) using a mixing time of 5 ms.

As the pseudo-contact shift of H^2_{nc} is positive, the magnetic axis must lie close to the line connecting Fe with H^2_{nc} (with positive $\Delta\chi_{ax}$) or orthogonal to it (with negative $\Delta\chi_{ax}$). We oriented the magnetic axis in such a way that it bisects the N-Fe-N angle. This results in an axial magnetic anisotropy $\Delta\chi_{ax}$ of +7 10^{-32} m^3 for **4**. Using this value and the geometric data of other H-atoms allows the pseudocontact contribution to be included for other signals of the molecule. This results in much better agreement of the experimental shifts with the calculated shifts as can be seen from Figure 4 in the main text. The alternative orientation of the magnetic axis and a negative $\Delta\chi_{ax}$ does not reproduce the experimental NMR values. We therefore conclude the orientation of the axis is indeed close to the line bisecting the N-Fe-N angle and that the magnetic anisotropy is positive.

For the Co complex (**3**), we were not able to identify the signal H^2_{nc}. However, using the same orientation of the magnetic axis and the same anisotropy as in **4** leads to an improvement of the correlation of

experimental and calculated NMR shifts. Starting from this value we fitted the size of $\Delta\chi_{ax}$ to +8 10^{-32} m^3 for **3** which leads to a very good correlation (see Figure 4 in the main text).

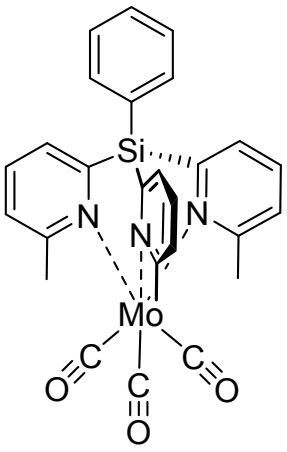

5

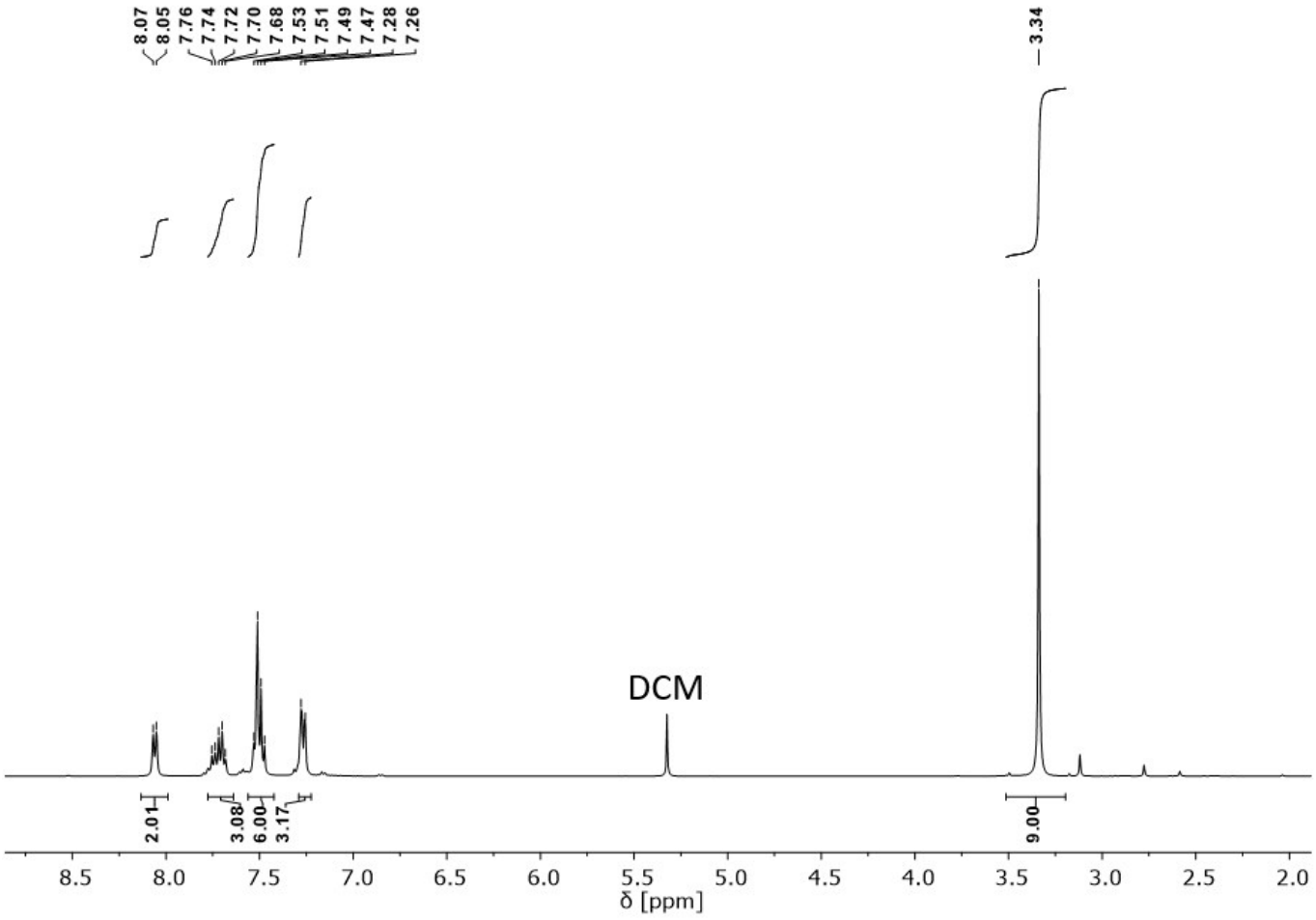

Figure S12: ^{1}H NMR spectrum (25°C, $CDCl_3$, 500.12 MHz) of **5**.

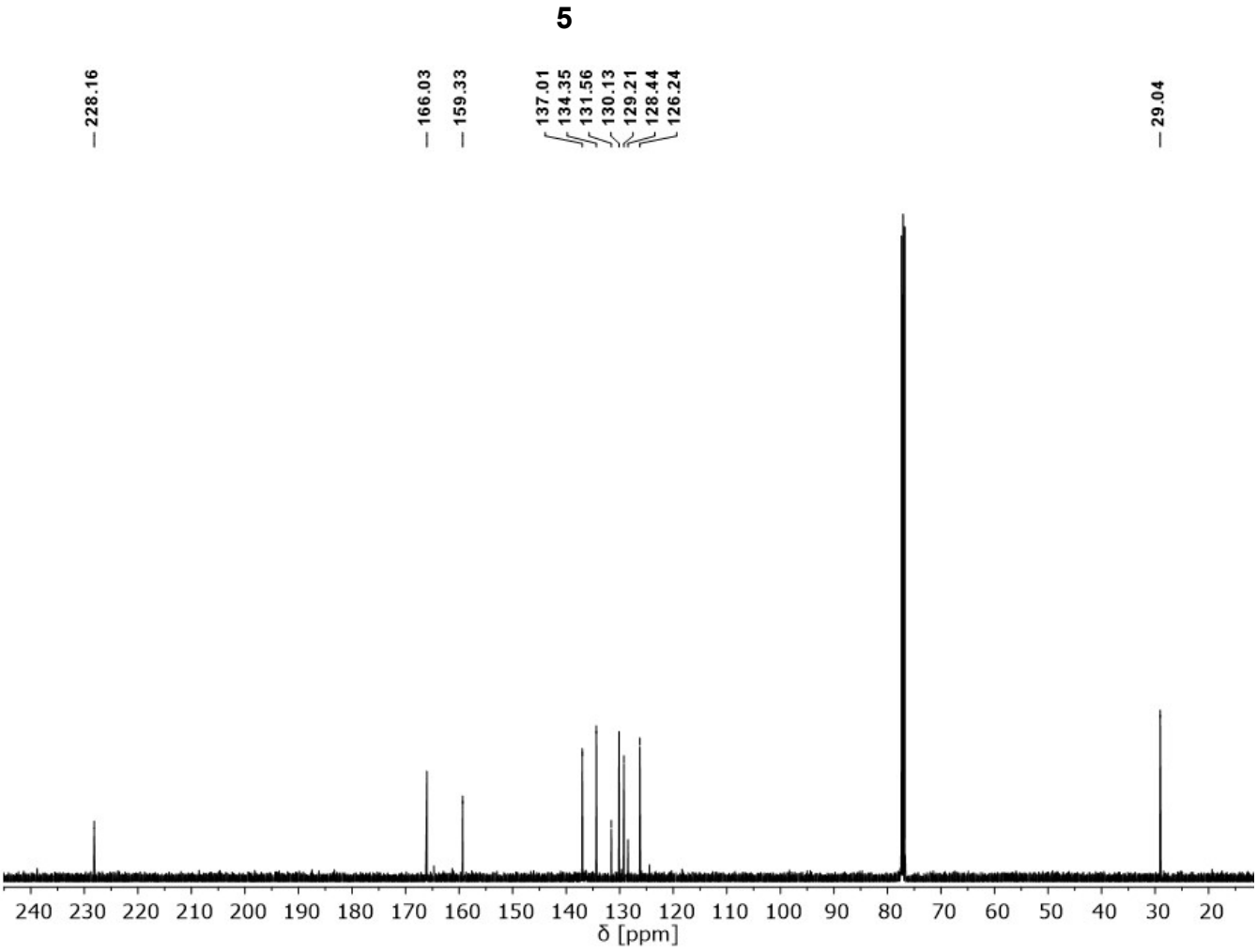

Figure S13: ^{13}C NMR spectrum (25°C, $CDCl_3$, 125.78 MHz) of **5**.

X-ray Crystallography

(CCDC 1833558-1833563)

Single-crystal X-ray diffraction data were collected at 180 K on a Bruker D8-QUEST PHOTON-100 diffractometer equipped with an Incoatec IμS Cu microsource (λ = 1.5418 Å). Data integration and reduction were carried out using SAINT within the APEX3 software suite. Multi-scan empirical absorption corrections were applied using SADABS. Structures were solved using SHELXT [2] and refined using full-matrix least squares on F^2 using SHELXL-2018/1 [3].

All structure refinements proceeded routinely.

$[\{PhSi(6\text{-}Me\text{-}2\text{-}py)_3\}Cu^{I}NCMe]^{+}Cu^{I}Cl_2^{-}$

The cation in $[\{PhSi(6\text{-}Me\text{-}2\text{-}py)_3\}Cu^{I}NCMe]^{+}Cu^{I}Cl_2^{-}$ lies on a crystallographic mirror plane, with the acetonitrile molecule and one 6-Me-2-py ring lying in the plane and the phenyl ring perpendicular to the plane. For both the 6-Me group and the Me group of MeCN, the H atoms were placed so that one H atom is on the mirror plane, and the other two are related to each other by the mirror plane.

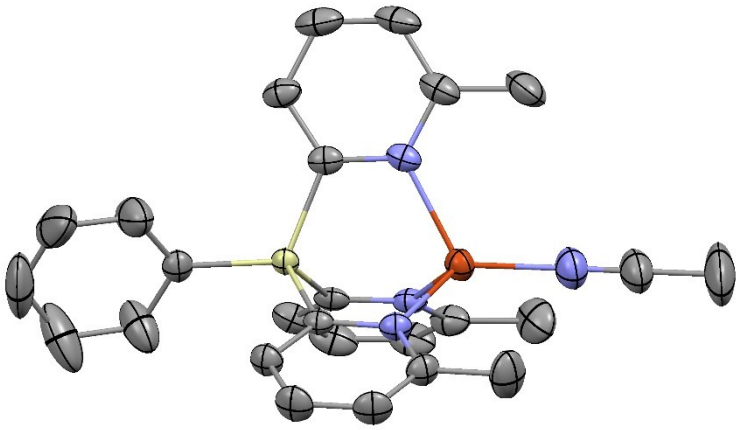

Figure S14: Structure of the cation $[\{PhSi(6\text{-}Me\text{-}2\text{-}py)_3\}Cu^{I}NCMe]^{+}$ with displacement ellipsoids shown at 50% probability and H atoms omitted. .Selected bond lengths (Å) and angles (°): Si–C_{phenyl} 1.867(4), Si–$C_{pyridyl}$ range 1.877(4)-1.894(3), Cu-$N_{pyridyl}$ range 2.068(3)-2.089(2), Cu-N_{MeCN} 1.948(4), $C_{pyridyl}$-Si-$C_{pyridyl}$ range 104.48(17)-108.61(11), Si-$C_{pyridyl}$-N range 114.0(2)-116.6(3), $N_{pyridyl}$-Cu-$N_{pyridyl}$ 95.38(13)-101.28(9). Colour key: Cu (red), Si (yellow), N (blue).

ESI Table 1. Crystal data and structure refinement details

	1	**2**	**3**	**4**	**5·CH_2Cl_2**	**[(1)Cu^{I}NCMe]$^{+}$$Cu^{I}Cl_2^{-}$**
CCDC number	1833561	1833563	1833559	1833560	1833562	1833558
Empirical formula	$C_{24}H_{23}N_3Si$	$C_{26}H_{26}CuF_6N_4PSi$	$C_{24}H_{23}Cl_2CoN_3Si$	$C_{24}H_{23}Cl_2FeN_3Si$	$C_{28}H_{25}Cl_2MoN_3O_3Si$	$C_{26}H_{26}Cl_2Cu_2N_4Si$
Formula weight	381.54	631.11	511.37	508.29	646.44	620.58
Temperature / K	180(2)	180(2)	180(2)	180(2)	180(2)	180(2)
Crystal system	monoclinic	monoclinic	monoclinic	monoclinic	triclinic	monoclinic
Space group	$P2_1/c$	$P2_1$	$C2/c$	$C2/c$	$P\,\bar{1}$	$P2_1/m$
a / Å	10.5199(3)	12.3186(4)	21.1277(5)	20.9935(5)	10.3558(3)	8.3554(2)
b / Å	10.5173(3)	8.3526(3)	10.1748(2)	10.2893(2)	10.5909(3)	14.2243(5)
c / Å	18.7496(5)	14.5003(4)	22.4008(5)	22.4986(5)	13.4578(4)	11.9797(3)
α / °	90	90	90	90	71.7724(11)	90
β / °	91.9156(13)	114.935(2)	93.7204(13)	93.9544(13)	87.4661(12)	106.219(2)
γ / °	90	90	90	90	77.4702(11)	90
Volume / Å^3	2073.31(10)	1352.90(8)	4805.35(18)	4848.32(18)	1368.11(7)	1367.12(7)
Z	4	2	8	8	2	2
ρ_{calc} / g cm^{-3}	1.222	1.549	1.414	1.393	1.569	1.508
μ / mm^{-1}	1.092	2.713	8.248	7.614	6.434	4.306
F(000)	808	644	2104	2096	656	632
Crystal size / mm^3	0.33×0.22×0.20	0.20×0.17×0.08	0.30×0.20×0.18	0.27×0.15×0.10	0.28×0.24×0.15	0.15×0.12×0.05
Radiation	CuKα (λ = 1.5418 Å)	CuKα (λ = 1.5418 Å)	CuKα (λ = 1.5418 Å)	CuKα (λ = 1.5418 Å)	CuKα (λ = 1.5418 Å)	CuKα (λ = 1.5418 Å)
2θ range / °	8.41 to 133.14	6.72 to 140.16	7.91 to 133.32	7.88 to 133.25	8.75 to 133.32	7.69 to 132.78
Reflections collected	13684	11757	11707	13623	13234	11500
Independent reflections	3646	4336	4194	4242	4787	2490
R_{int}	0.0397	0.0414	0.0304	0.0397	0.0415	0.0377
Goodness-of-fit on F^2	1.05	1.08	1.02	1.03	1.10	1.04
Data/restraints/parameters	3646/0/256	4336/1/356	4194/0/283	4242/0/283	4787/0/346	2490/0/182
*R*1 [*I*>2σ(I)]	0.0422	0.0388	0.0327	0.0340	0.0335	0.0424
w*R*2 [all data]	0.1114	0.0954	0.0798	0.0838	0.0834	0.1067
Largest diff. peak/hole / eÅ^{-3}	0.35/-0.36	0.70/-0.36	0.27/-0.39	0.33/-0.36	1.17/-0.89	0.51/-0.40
Flack Parameter		0.01(3)				

Literature

[1] M. J. Frisch; G. W. Trucks; H. B. Schlegel; G. E. Scuseria; M. A. Robb; J. R. Cheeseman; G. Scalmani; V. Barone; B. Mennucci; G. A. Petersson; H. Nakatsuji; M. Caricato; X. Li; H. P. Hratchian; A. F. Izmaylov; J. Bloino; G. Zheng; J. L. Sonnenberg; M. Hada; M. Ehara; K. Toyota; R. Fukuda; J. Hasegawa; M. Ishida; T. Nakajima; Y. Honda; O. Kitao; H. Nakai; T. Vreven; J. A. Montgomery, J.; J. E. Peralta; F. Ogliaro; M. Bearpark; J. J. Heyd; E. Brothers; K. N. Kudin; V. N. Staroverov; T. Keith; R. Kobayashi; J. Normand; K. Raghavachari; A. Rendell; J. C. Burant; S. S. Iyengar; J. Tomasi; M. Cossi; N. Rega; J. M. Millam; M. Klene; J. E. Knox; J. B. Cross; V. Bakken; C. Adamo; J. Jaramillo; R. Gomperts; R. E. Stratmann; O. Yazyev; A. J. Austin; R. Cammi; C. Pomelli; J. W. Ochterski; R. L. Martin; K. Morokuma; V. G. Zakrzewski; G. A. Voth; P. Salvador; J. J. Dannenberg; S. Dapprich; A. D. Daniels; O. Farkas; J. B. Foresman; J. V. Ortiz; J. Cioslowski; Fox, D. J. Gaussian 09, Revision D.01, Gaussian, Inc., Wallingford CT, 2013.

[2] G. M. Sheldrick (2015). Acta Crystallogr. A71, 3–8.

[3] G. M. Sheldrick (2015). Acta Crystallogr. C71, 3–8.